AGU100 ADVANCING EARTH AND SPACE SCIENCE

Water Resources Research

RESEARCH ARTICLE
10.1029/2017WR021681

The Influence of Syndepositional Macropores on the Hydraulic Integrity of Thick Alluvial Clay Aquitards

Wendy A. Timms[1,2], R. Ian Acworth[2,3], Richard A. Crane[1,4], Christoph H. Arns[5], Ji-Youn Arns[6], Dayna E. McGeeney[2,3], Gabriel C. Rau[2,3], and Mark O. Cuthbert[2,7]

[1]School of Mining Engineering, University of New South Wales, Sydney, NSW, Australia, [2]Connected Waters Initiative Research Centre, University of New South Wales, Sydney, NSW, Australia, [3]Water Research Laboratory, School of Civil and Environmental Engineering, University of New South Wales, Sydney, NSW, Australia, [4]Camborne School of Mines, College of Engineering, Mathematics and Physical Sciences, University of Exeter, Penryn, UK, [5]School of Petroleum Engineering, University of New South Wales, Sydney, NSW, Australia, [6]Department of Applied Mathematics, Research School of Physics and Engineering, Australian National University, Canberra, ACT, Australia, [7]School of Earth and Ocean Sciences, Cardiff University, Cardiff, UK

Key Points:
- Syndepositional macropores generated in a paleo soil can increase pore connectivity and therefore the vertical hydraulic conductivity
- Syndepositional macropores are present at greater depths than postdepositional features which are more prevalent in the near surface
- The scale of the macropores is of the order of millimeter and likely represents paleo root channels and/or biological pathways

Correspondence to:
W. Timms,
w.timms@unsw.edu.au

Citation:
Timms, W. A., Ian Acworth, R., Crane, R. A., Arns, C. H., Arns, J.-Y., McGeeney, D. E., et al. (2018). The influence of syndepositional macropores on the hydraulic integrity of thick alluvial clay aquitards. *Water Resources Research*, *54*, 3122–3138. https://doi.org/10.1029/2017WR021681

Received 9 AUG 2017
Accepted 31 MAR 2018
Accepted article online 6 APR 2018
Published online 26 APR 2018

Abstract Clay-rich deposits are commonly assumed to be aquitards which act as natural hydraulic barriers due to their low hydraulic connectivity. Postdepositional weathering processes are known to increase the permeability of aquitards in the near surface but not impact on deeper parts of relatively thick formations. However, syndepositional processes affecting the hydraulic properties of aquitards have previously received little attention in the literature. Here, we analyze a 31 m deep sediment core recovered from an inland clay-rich sedimentary sequence using a combination of techniques including particle size distribution and microscopy, centrifuge dye tracer testing and micro X-ray CT imaging. Subaerial deposition of soils within these fine grained alluvial deposits has led to the preservation of considerable macropores (root channels or animal burrows). Connected pores and macropores thus account for vertical hydraulic conductivity (K) of 4.2×10^{-9} m/s (geometric mean of 13 samples) throughout the thick aquitard, compared to a matrix K that is likely $<10^{-10}$ m/s, the minimum K value that was measured. Our testing demonstrates that such syndepositional features may compromise the hydraulic integrity of what otherwise appears to have the characteristics of a much lower permeability aquitard. Heterogeneity within a clay-rich matrix could also enhance vertical connectivity, as indicated by digital analysis of pore morphology in CT images. We highlight that the paleo-environment under which the sediment was deposited must be considered when aquitards are investigated as potential natural hydraulic barriers and illustrate the value of combining multiple investigation techniques for characterizing clay-rich deposits.

1. Introduction

Clay-rich deposits are often considered to behave as aquitards and protect underlying aquifers from aqueous contamination. In such instances, aquifer protection is typically assumed to be provided by thick homogeneous clay sequences through which solute transport is slow since it is governed primarily by molecular diffusion. Many studies of clay-dominated aquitards have, however, documented features that serve as preferential flow paths permitting significant flow via advection, including biogenic channels (Hinsby et al., 1996; Jorgensen et al., 2002; Vulava et al., 2007), discrete silt or sand layers (Cuthbert et al., 2009; Wealthall et al., 2001), desiccation cracks (Cuthbert et al., 2010; Wealthall et al., 2001), fractures (Greve et al., 2010a; McKay et al., 1993; Rudolph et al., 1991), and paleo organic matter (White et al., 2008). Indeed, preferential flow paths have been documented to exhibit a hydraulic conductivity (K) several orders of magnitude faster than the surrounding matrix. For example, McKay et al. (1993) measured a range for horizontal K of 10^{-6} to 10^{-10} m/s, with preferential flow pathways through a glacial till identified as fractures to a depth of 6 m below ground level (BGL) and roots, root casts, and fractures to depths of 3–4 m BGL. Rudolph et al. (1991) noted that preferential flow paths with apertures of 30 μm could explain deep movement of water in an aquitard above an important aquifer in Mexico City.

Buried paleosols are reported in the literature; however, no reports of macropores within buried paleosols have been identified. Paleosols within loess were reported in Southwest Germany, where the uppermost 9.5 m of a late Pleistocene loess paleosol was investigated (Gocke et al., 2017). In an area of Washington and Idaho, Busacca (1989) reported multiple buried paleosols up to 75 m deep acting as restrictions to flow.

These thick loess deposits consisting of paleosol sequences, were evaluated to 6 m depth using environmental tracers (O'Geen et al., 2005), with no reports of macropore flow.

Where preferential flow pathways do penetrate through an otherwise low-permeability unit, they can act as highly efficient conduits for groundwater recharge (Acworth & Timms, 2009; Cuthbert & Tindimugaya, 2010). Vertical connectivity could also be enhanced by textural heterogeneity, particularly if there are sufficient coarser grained deposits to provide a flow pathway. The availability of pathways for fluid flow and contaminant transport enhances hydraulic connectivity. Connectivity through preferential flow can lead to more complex, and therefore expensive, remediation scenarios, and could have implications for mining or coal seam gas development that relies on a competent flow barrier to limit surface impacts.

Hence, understanding the origin and nature of preferential flow in aquitards is critical in order to successfully manage groundwater resources, with a key concern being to determine the depth BGL at which such features can occur. The majority of studies to date have investigated aquitards where preferential flow pathways were formed via post depositional processes. In such instances, preferential flow pathways typically propagate from the surface (e.g., fracturing due to stress relief on unloading, dessication cracks, rootholes, biogenic channels) and are therefore mostly restricted to the top few meters of the aquitard (Klint & Gravesen, 1999; O'Hara et al., 2000). In contrast, there have been few investigations to date on the influence of syndepositional preferential flow pathways (i.e., paleorootholes, paleosols, tectonic fractures) on aquitard hydraulics (Emanuel & Sapsford, 2016; Jorgensen et al., 1998; Neuzil, 1994; White et al., 2008). In such scenarios, preferential flow pathways are formed during aquitard deposition (e.g., vegetation growth and associated root holes that are pervasive or provide channels) and are buried as the aquitard deposits accumulate. While it is likely that increasing confining stress during aquitard burial would result in an associated decrease in the permeability of such features, in theory, it is possible that hydraulically active features could remain present independent of depth under suitable depositional and diagenetic conditions. For example, hydraulically active features may be retained if loads and stresses on the sediments at the site do not exceed preconsolidation stresses that have been determined from geotechnical analysis of core samples from this site (Bouzalakos et al., 2016).

Investigations of a 31 m deep clayey silt paleovalley fill from Cattle Lane, Australia (Acworth et al., 2015), have revealed the potential for hydraulically active flow paths. Geotechnical centrifuge techniques (Crane et al., 2015; Timms et al., 2016) found that vertical K varied between 1.4×10^{-8} and 1.1×10^{-10} m/s with a geometric mean value of 4.2×10^{-9} m/s (13 samples, 5–31.4 m BGL), values that were consistent with in situ vertical K values (Timms & Acworth, 2005). The vertical K values are high for an aquitard (as defined by K of $10^{-8}-10^{-16}$ m/s; Neuzil, 1994) and have prompted more detailed investigation into the depositional properties and groundwater processes at this site.

The valuable agricultural soils at the site and buried paleosols are part of a regionally extensive sheets of smectite-dominated material, weathered from Paleocene volcanics. In this region, smectite clays overlie sand and gravel alluvium (that contain fresh groundwater) that occur in early Cenozoic erosional valley systems cut into Permo-Triassic sandstone, shale, and coal deposits. The agricultural and mining sectors are frequently in competition over land use and water resources in this region.

In this paper, we analyze in detail parts of a sediment core from the clayey silt sequence at Cattle Lane, Australia. We consider hydraulic connectivity with multiscale techniques including dye tracing and analysis of particle size and heterogeneity. Connectivity is also described by quantitative measures including: a connectivity threshold based on drill hole lithology logs at site scale; vertical hydraulic conductivity of the aquitard at the site; and digital core analysis using micro X-ray CT technology that indicates connectivity of pores.

The results are then integrated with previous findings on the vertical hydraulic conductivity as well as age dating that indicate that aquitard integrity may be compromised by syndepositional macropores. Our results have significant implications for the consideration of aquitards as natural hydraulic barriers.

2. Methodology

2.1. Field Site and Previous Work

The core samples and groundwater used in this study were sourced from the Cattle Lane research site (Lat: −31.5166, Long: 150.4686), which is located (Figure 1) on the Liverpool Plains of northern New South Wales in Australia.

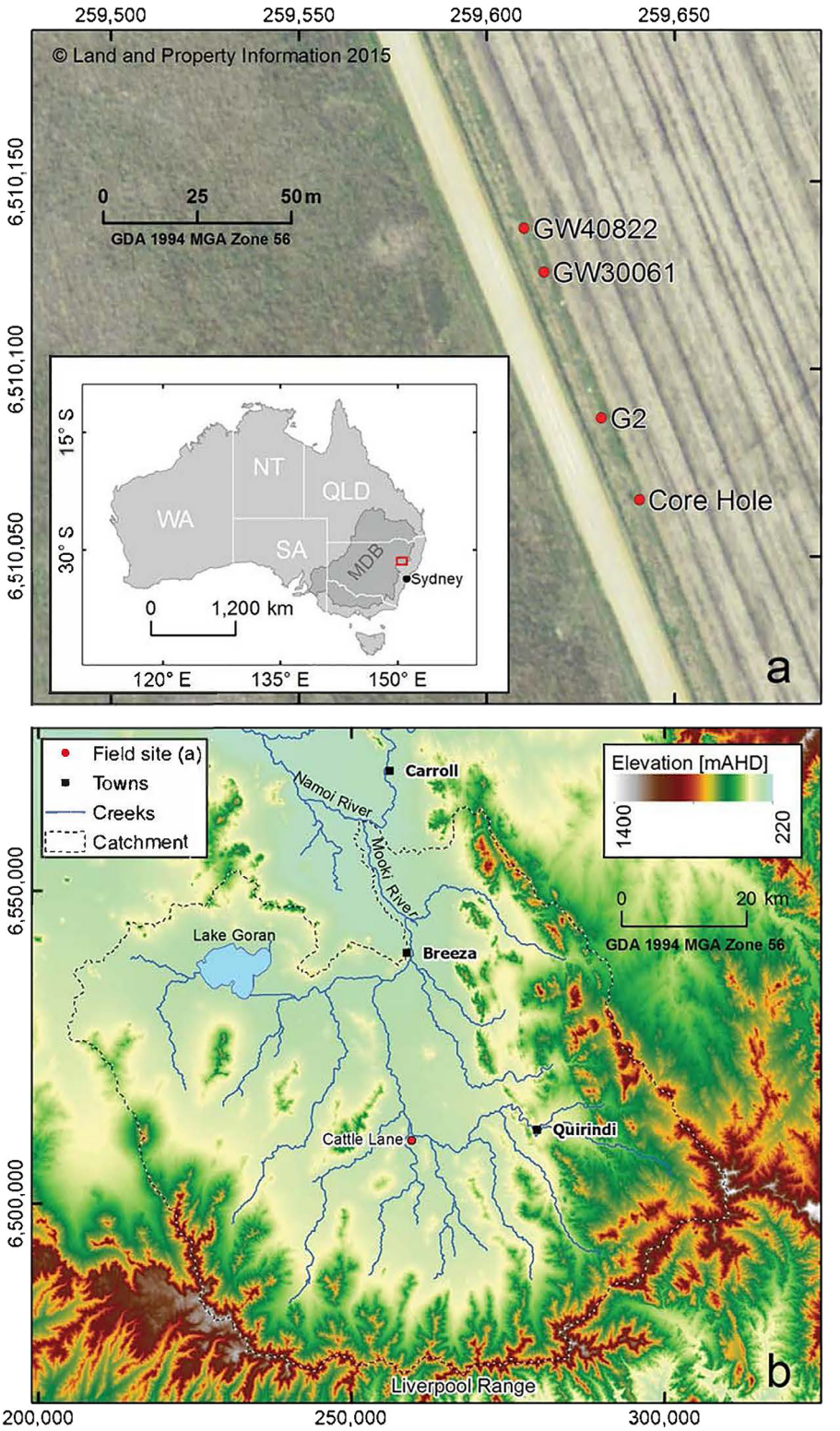

Figure 1. Map showing the location of the field site in Australia (inset a): (b) Cattle Lane on the Liverpool Plains and (a) the boreholes used in this investigation.

An initial bore was drilled at the site in 1978 (GW 30061) to basement at 102 m, then backfilled to 56 m and completed as a piezometer. Additional piezometers (GW 40822-1, −2, −3, and −4) were completed in 1998 (Acworth & Timms, 2009) to characterize the aquifer and overlying clay-dominated material. In 2012, a

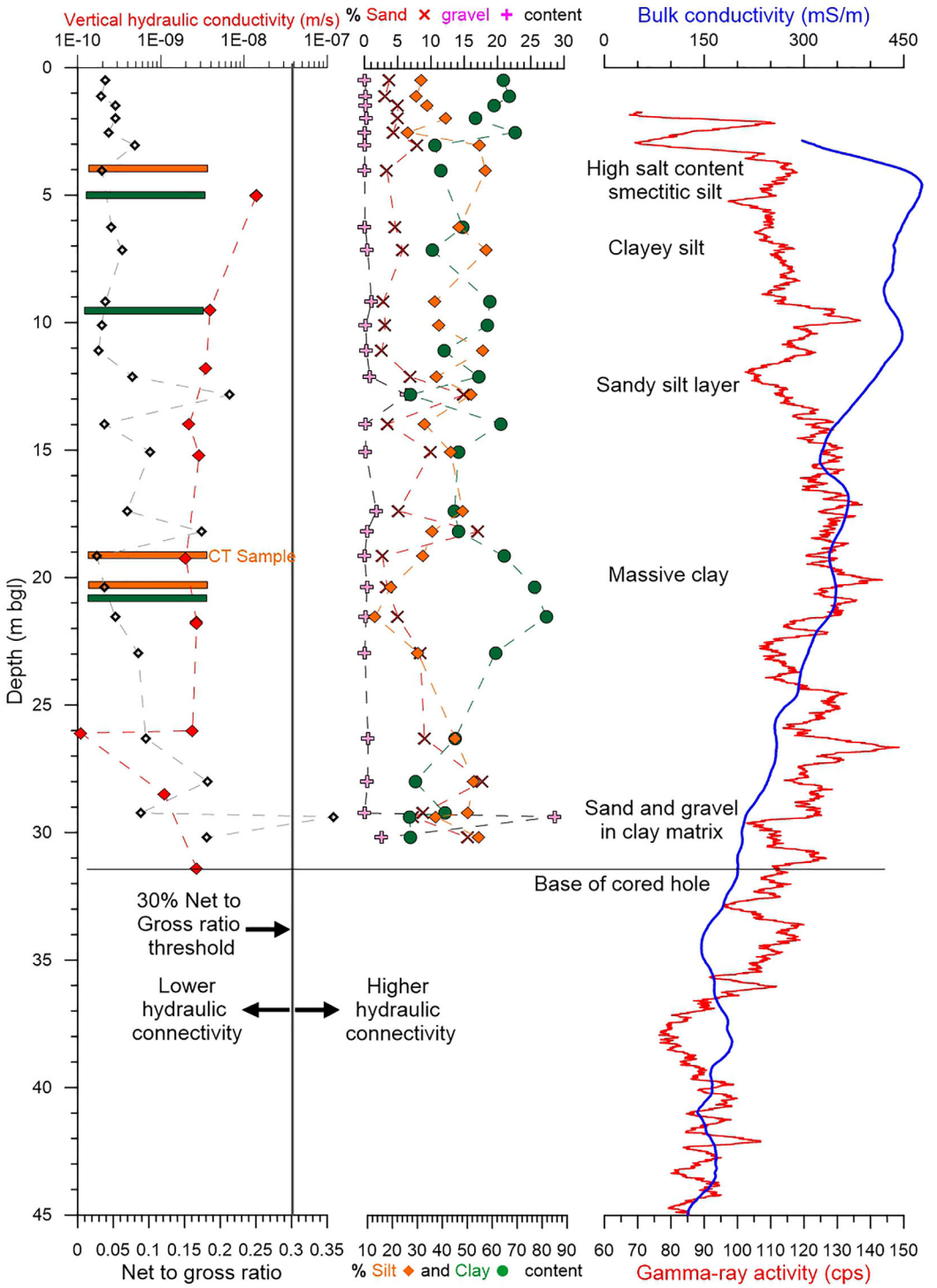

Figure 2. Plot to show existing data sets previously reported (Acworth et al., 2015) and of significance to this study as they provide important contextual information. The locations of samples described in detail in this paper are shown by orange bars (PSD and CT testing) or green bars (dye testing) on the first plot. This also shows net to gross ratio data for the entire sequence and the values of vertical hydraulic conductivity determined by centrifuge testing. The second plot shows particle size distribution data. The third plot shows bulk electrical conductivity and gamma-ray activity data obtained by geophysical logging in an adjacent bore (G2), with lithological comments recorded at the time of drilling and sampling.

continuous core was recovered (Core hole on Figure 1) to ≈31.5 m using a Treifus triple-tube core barrel (Acworth et al., 2015). The core barrel was 1.5 m long but as the cores were collected by pushing the central tube down while rotating the outer drill bit, the formation resistance was sometimes too great to completely fill the 1.5 m barrel. A total of 21 cores in 1.5 m lengths (maximum) were recovered directly into the 101.6 mm ID clear PVC core tubes used to line the Treifus barrel (Timms et al., 2016). Geophysical logging was completed for all the bores. The logs shown on Figure 2 are from Borehole G2, close to the core hole.

Further details on methods to minimize disturbance to the cores during sampling and laboratory testing are detailed by Timms et al. (2016). Minimizing structural and moisture changes to these clayey cores was important for reliable characterization of macropores and hydraulic connectivity.

A graphical summary of some of this earlier work is presented in Figure 2 to provide overall context for the location of sediment samples described in this study. The entire 31 m sequence at Cattle Lane has previously been dated, using a combination of radio-carbon and optically stimulated luminescence, to be younger than approximately 120 ka (Acworth et al., 2015).

The depth to the saturated zone at this site is less than a meter or two below ground (Acworth et al., 2017; Timms & Acworth, 2005). Pore pressures within the clay sediments respond to barometric and earth tide strains and loading of moisture within the surface soils (Acworth et al., 2016, 2017). Swelling during wetting of these smectite soils was observed to close surface cracks that were up to 30 mm wide, resulting in a more homogeneous soil (Greve et al., 2010b, 2012). A transition from crack flow to matrix flow in response to increasing moisture occurred at depths of at least 0.5 m from the surface during laboratory experiments (Greve et al., 2012). Dye tracing of cores in this study were from depths below the saturated zone and surface cracking.

2.2. Particle Size Distribution

Samples used for particle size distribution (PSD) analysis were obtained from the nonrotating shoe at the cutting end of the core barrel to avoid disturbing each core within the liner. Each sample with a mass of ≈40 g was air dried for 28 days and then immersed in 100 mL of Milli-Q water (>18.2 MΩcm) and then sonicated for 60 minutes using a Soniclean 120T. Approximately 400 mL of Milli-Q water was added and the resultant slurry mixed in a rotary tube mixer at 10 rpm for 60 min. The slurry was then centrifuged at 1,000 g and the supernatant removed. Approximately 450 mL of Milli-Q water and 50 mL of 25% sodium hexametaphosphate were then added and mixed using a rotary tube mixer at 10 rpm for 16 h. Sieve analysis from 11,200 to 45 μm aperture size was performed. A Malvern Mastersizer 2000 laser diffraction was used to quantify particle size distribution $<$ 45 μm. PSD data were analyzed using GRADISTAT v.8.0 (Blott & Pye, 2001).

The sorted bins from the PSD evaluations (45, 63, 125, 250, 500, and 1,000 μm) have been examined under the microscope and photographed to assist with visual particle identification. Note was made of mineral identification, root and shell remains, and the presence of charcoal during this process. Analysis of the clay mineralogy of each PSD bin was not considered because XRD results previously reported indicated the dominance of smectite clay (and minor illite) in all samples from the site (Acworth et al., 2015).

2.3. Dye Tracer Testing and Sample Dissection

Steady state *K* measurements of core subsamples taken from 5.0, 9.5, and 21.8m depth BGL (below ground level) were reported by Crane et al. (2015) and Timms et al. (2016). Details are provided on steps to ensure reliable *K* measurements of intact samples (Crane et al., 2015; Timms et al., 2016), primarily related to core storage, stress application and detection of rapid leakage. Potential errors were evaluated and minimized for example, by using relatively large diameter cores (101.6 mm) and application of stresses less than or equivalent to in situ stresses at the depth of core collection.

After those *K* measurements were complete, separate dye tracing tests were completed on these core subsamples for this study. A visual (blue) dye tracer (Premier Pty Ltd., dye identification number 192004) was added to their influent lines at a concentration of 0.1 g/L, and the samples were centrifuged until breakthrough of the dye was observed in the effluent. Breakthrough occurred at times of 4, 48, and 24 hours, respectively. The core samples were then removed from the centrifuge permeameter, dissected into discrete sections and photographed. The cores were allowed to break along predisposed planes of weakness.

2.4. Micro X-Ray CT Image Acquisition and Analysis

Micro X-ray CT imaging and digital core analysis (Arns et al., 2005a) were carried out on a single core subsample taken from the base of Core 13 (18.0–19.5 m). This depth corresponded with clay from approximately 74 ka years (Acworth et al., 2015), with a vertical hydraulic conductivity that was typical for this sequence (Figure 2). The vertical hydraulic conductivity of this sample had previously been determined as 2.0×10^{-9} m/s (Timms et al., 2016). It is worth noting that drilling and sampling proceeded between 16.5 and 24.0 m (Cores 12 to 16), through massive clay (Figure 2), with 100% core recovery.

A 34 mm high section of the middle region of the sample (diameter 101.6 mm, 80 mm length) from a depth of 19.17 to 19.25 m BGL was selected for imaging. This section was selected as a large macropore was apparent during initial low-resolution CT scanning of the core after centrifuge permeameter testing. The soil was kept wet by sealing the sample in a special core holder. The core was imaged in circular acquisition mode on the custom-built UNSW Tyree X-ray CT facility with a 1 mm stainless steel filter to reduce imaging artifacts. A tomogram with voxel size of ϵ^3, ϵ=49 μm was recorded using a flat panel detector of 3040 $\times$ 3040 pixels. The moderate resolution of CT imaging in this case was selected to characterize the morphology of millimeter-scale features within a relatively large clay soil core (34 mm high section). By contrast, previous studies with higher-resolution micro CT images used smaller cores that could not evaluate large-scale features. For example, the relationship between the resolution of micro-CT images that was possible on sandstone cores 5 to 25 mm diameter was investigated by Botha and Sheppard (2016).

Initial beam hardening and ring artifacts in the tomographic images were removed using Gaussian-based filters. The reconstructed tomogram was segmented into soil matrix, water-filled pore regions, and gas-filled large pore regions using the techniques described by Sheppard et al. (2004) and Arns et al. (2005a). The combined gas and water-filled pore space in the 3-D segmented image was then used to determine 3-D topology and geometry of the pore space. A pore-throat network was extracted from the combined gas and water phases to facilitate analysis of local pore geometry and the associated topology (connectivity) in 3-D pore space (Arns et al., 2007). The extraction method of the pore-throat geometry and topology originates from the drainage flow displacement mechanism observed on glass models by Lenormand et al. (1983). In particular, a nonwetting phase (i.e., gas) invading the pore space does so in a series of events, with large throats being traversed first by the nonwetting fluid.

Local surface roughness affects pore network extraction and often produces unnecessary small pores. Regional merging is performed for the medial-axis-based network extraction method (Arns et al., 2007). In this work a 3D covering radius extraction method operating on the Euclidean distance map is used. This algorithm is described in detail by Arns et al. (2005b). The process can be visualized by considering the deep valleys (largest distances) of the distance map as start (seed) regions for converging active contours, which then partition the pore space into pores. The resulting network is analyzed in terms of coordination number distribution (number of connections for each pore), mean pore diameter, mean throat diameter, and pore-throat aspect ratio (Sheppard et al., 2005). The large-scale porosity regions were visualized using the Drishti package (Limaye, 2012).

3. Results

3.1. Particle Size Distribution (PSD) Results

The net-to-gross ratio derived from particle size results of core samples as a function of depth BGL is displayed in Figure 2, where net denotes the sand plus gravel (particle size $>$63 μm) fractions and the gross is the total volume. The 30% hydraulic connectivity threshold (Larue & Hovadik, 2006) is shown as a vertical black line. Above 0.3, a relatively higher hydraulic connectivity between stacked sand (particle size 63–2,000 μm) and gravel (2,000–64,000 μm) bodies is assumed. Below 0.3, there is a relatively low hydraulic connectivity between such particles due to the presence of relatively large concentrations of silt (particle size 2–63 μm) and clay (particle size $<$2 μm) particles and the improbability of pore interconnection that would allow fluid migration.

The net-to-gross ratio is low in the Cattle Lane core to a depth of 12 m. This correlates with sustained high values ($>$400 mS/m) of bulk electrical conductivity (Figure 2). Three intervals below 12 m show thin lenses of increased net-to-gross ratio with a trend beneath 26 m of increasing values. The coarser grained and isolated thin lenses indicate some textural heterogeneity in an otherwise fine grained aquitard. An average

net-to-gross ratio of 0.09 was recorded for the core to a depth of 30.18 m BGL. Clay sized particles are typically dominant (Figure 2, center) at around 60%–80%, while the combined silt and clay fraction is around 0.91 from ground surface to 30 m depth.

It would typically be concluded that the core represented low hydraulic conductivity material, typical of an aquitard. Comparison of *K* values and particle size variations with depth (Figure 6) reveals minor differences in the proportion of silt relative to clay in sediments with depth, but little difference in the proportion of sand plus gravel (net) to fine sediments (gross). The variations in net-to-gross ratio that increases with depth, do not appear to coincide with decreasing *K* values as would be expected if textural heterogeneity were the primary factor in *K* average of 10^{-9} m/s for the 31 m thick aquitard. It is therefore reasonable that macrapores and connected pores are the primary reason for the relatively high *K* values through this aquitard, although textural heterogeneity could also be a factor, particularly in pore-throat connectivity (section 3.3).

A picture of the material dried before PSD is also shown along with the grain-size plot. The PSD analyses for material at 4.5 m depth are shown in Figure 3. This was the sample closest to the first core used for the dye breakthrough test described below. PSD analyses are shown for the closest samples from both above and below the depth (19.25 m) in which the core selected for detailed CT scanning occurred. These data are shown in Figure 4.

3.2. Dye Tracer Results

Figure 5 displays photographs of the dissected cores following dye permeation for core samples taken from 5.0, 9.5, and 21.8 m BGL (Crane et al., 2015).

For all samples, the dye was observed to lie along discrete sinuous and small-scale (<1 mm) channels. The width of the stained area around the channels appears to be smallest in the sample from 5 m, and becomes progressively larger for the samples from greater depths. This observation is most probably explained by the lower hydraulic conductivity (Figure 2) of the deeper samples that required longer time for the tests to be conducted. The longer time period allowed greater diffusive mass transfer of the dye tracer into the surrounding matrix away from the channel. Unfortunately due to the destructive nature of examining the macropores after all *K* and dye tests were complete, it was not possible to examine natural color characteristics.

3.3. Micro CT-Based Sample Characterization

Figure 6 shows the digital image processing procedure performed starting with the reconstructed 3-D tomogram image to completion of pore partitioning and network generation and depicting a horizontal slice through the sample at 19.25 m depth. There are clear voids visible within the sample that could not have been created after sample removal without damaging the surrounding core. The reconstructed tomogram in Figure 6a was segmented into soil matrix, water-filled pore regions, and gas-filled large pore regions. Figure 6b shows the intensity histogram of the 3-D tomogram with total intensity in black and individual intensity distributions, segmented as phases such as gas, water, clay and others. The overlapping intensity distributions of water and gas are well separated and the resultant segmented fluid phases clearly shown (Figure 6c). A close-up of the enclosed gas bubble is given in Figure 6d) and demonstrates the characteristic fluid-gas curved boundaries for gas as nonwetting phase, giving further confidence in the robustness of the segmentation. The volume fractions identified for each phase are summarized in Table 1, indicating that the majority of the core section was soil (i.e., clay and matrix). Porosity was mostly water filled (0.138), plus a component of gas-filled porosity (0.012).

The Euclidean distance map as basis for pore network extraction, derived on the union of the gas and water-filled pore space, is depicted in Figure 6e. The brightest voxels in the Euclidean distance map denote the distances furthest from the solid (i.e., the center of the pore space) and the darkest are nearest to the solid (i.e., close to the surface of the solid). Finally, Figure 6f shows the pore label field, which together with the network statistics given in Figure 7 is an output of the network extraction algorithm.

The statistics of the extracted pore network partition are shown in Figure 7c. Typical homogeneous sandstone has a coordination number (connectivity of pore network) of about 3.5. The statistics of the current sample shows about 4.8 with a standard deviation of 4.31, indicating a well-connected heterogeneous pore structure which is more characteristic of carbonate-dominated systems (Knackstedt et al., 2006). Heterogeneity is also evident through the broad distribution of pore and throat size in Figures 7a and 7b. The high

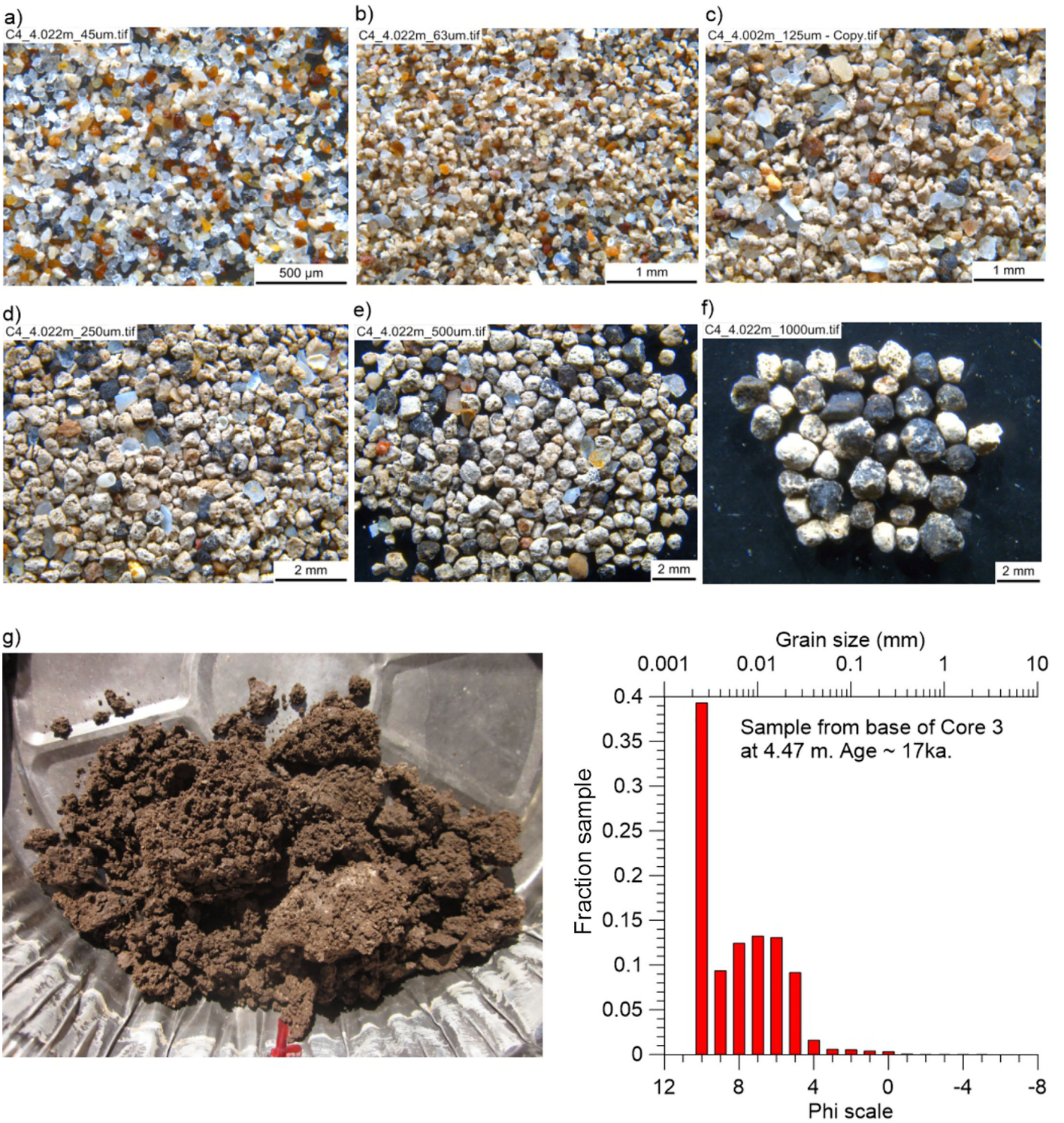

Figure 3. Clayey silt from 4.5 m depth. Photomicrographs are of the PSD sample at (a) 45 μm, (b) 63 μm, (c) 125 μm, (d) 250 μm, (e) 500 μm, and (f) 1,000 μm. The sample after drying and prior to the PSD is shown in Figure 3g. The final image is the PSD analysis. The pale white fragments are calcrete that has been first deposited in the weathered zone of the calc-alkali volcanics of the Liverpool Ranges and then eroded and transported northward onto the Liverpool Plains. The blue grains are quartz, added to the sediment sequence either as dust or as erosion products from the adjacent Triassic Sandstone hills.

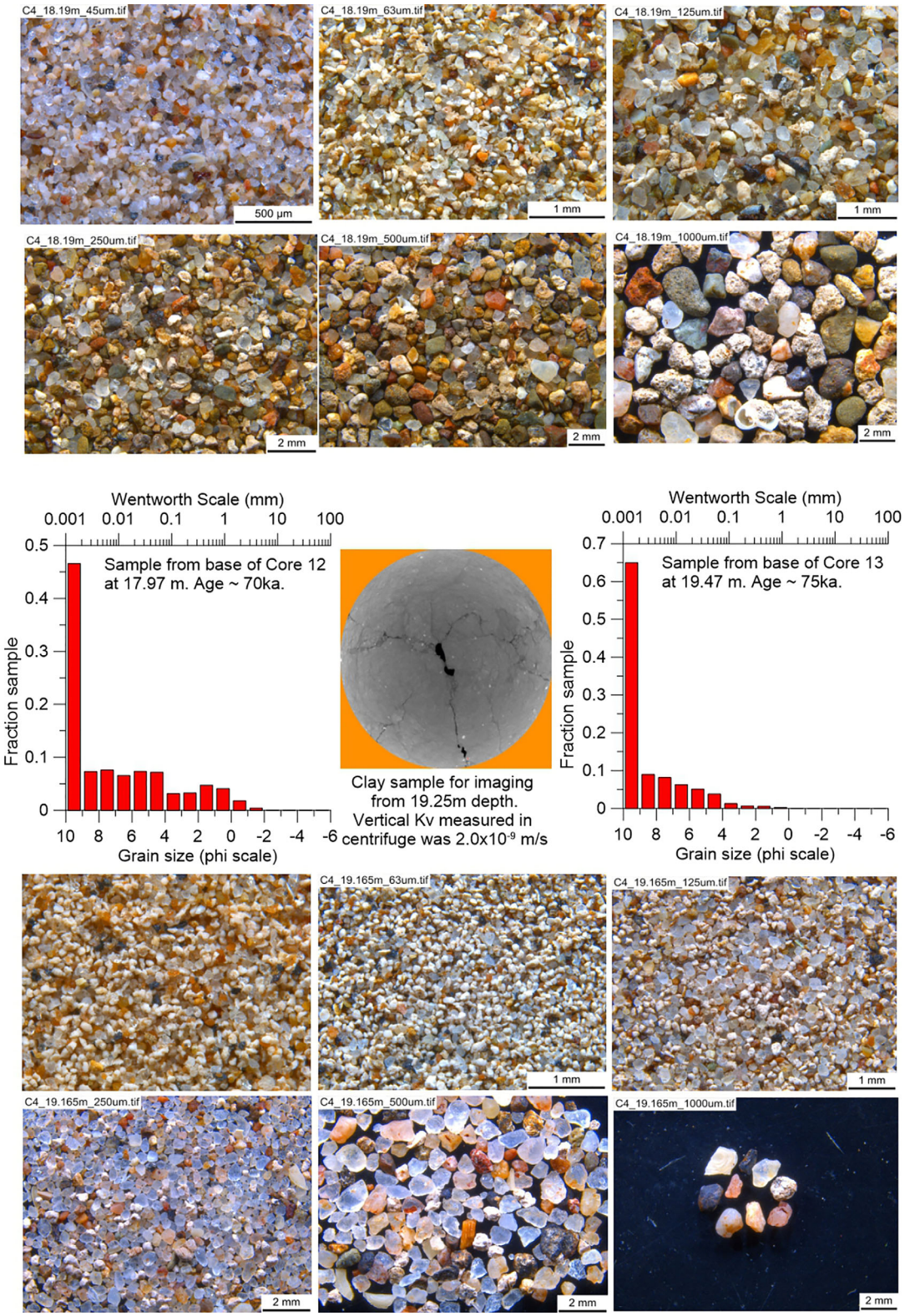

Figure 4. PSD data from above (Core 12 at 17.97 m) and below (Core 13 at 19.47 m) the depth of 19.25 m where the CT scan image sample was taken. The material is predominantly (>60%) clay with embedded quartz, mineral, and calcrete fragments. The order of the photomicrographs follows that given in Figure 3. The central image is a CT scan of the core sample at 19.25 m that is shown in greater detail in Figure 6.

aspect ratio, calculated from the ratio of local pore and throat size in Figure 7d, may cause rate sensitive displacement patterns. In addition, the low coordination number may indicate channel-like pores that may have been generated by roots, albeit no root material was present in the sample studied. The tail toward high coordination numbers reflects large pores (vugs), which are connected to many of the smaller pores. The distributions observed are typical for more heterogeneous samples exhibiting a wider coordination number distribution.

The mean coordination number from CT imaging is a natural measure of pore connectivity (i.e., the average number of channels connected to a nodal pore). However, Bernabe et al. (2016) consider that a number of scale-invariant factors (i.e., properties that do not change if length scales are multiplied by a common factor) could also contribute to connectivity including pore shape, orientation, and pore-scale heterogeneity. Heterogeneity and connectivity are particularly important factors for the permeability model of Bernabe et al. (2016). However, consideration of such models for permeability and connectivity, based on measurements during CT imaging, are beyond the scope of this paper.

Figure 8 indicates that the center of the core sample contains a very large macropore (millimeter scale), which is gas filled. We note that while the pore network is connected to the outside, a percolation check (Hoshen & Kopelman, 1976) on the gas phase demonstrates that this pore is not connected to the outside of the sample. It appears however, that this macropore is similar to the preferential flow paths identified by dye tracing (Figure 5).

4. Discussion

4.1. Origin of the Sediments

Acworth et al. (2015) previously presented dates derived from optical luminescence studies (Figures 3 and 4) for the core material further investigated in this paper. The sample from 4 m depth represents 17 ka old

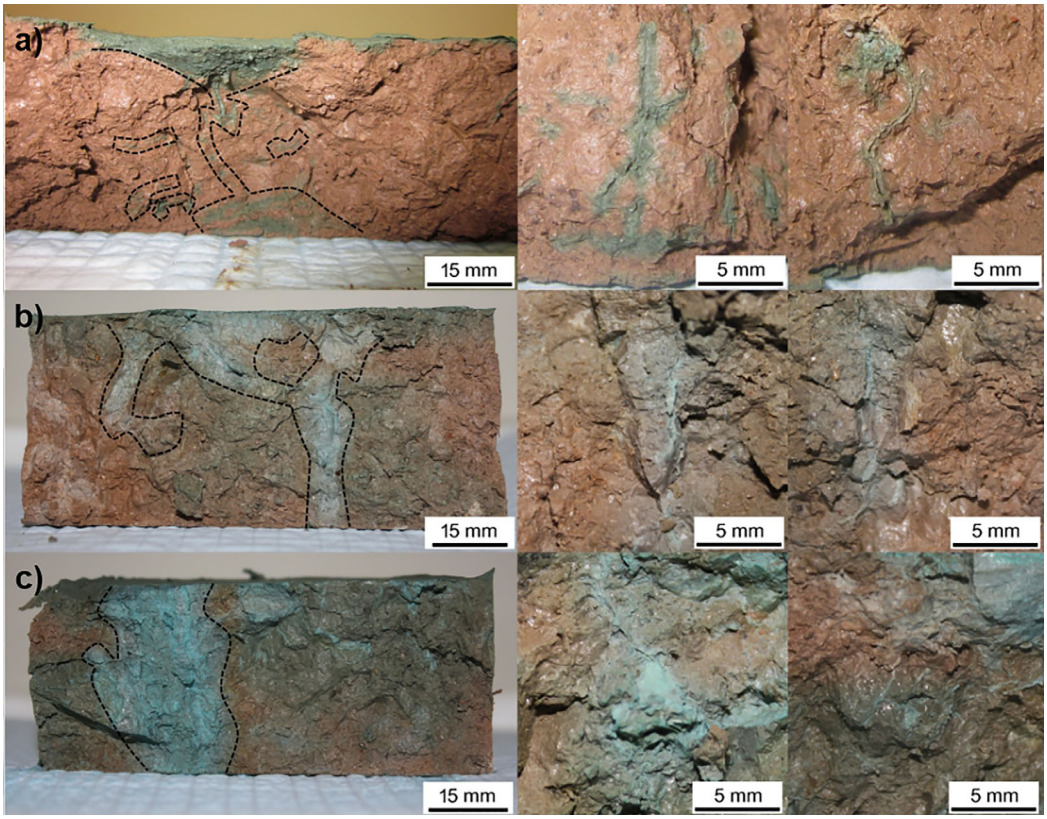

Figure 5. Cores and close-up of core after dye breakthrough: (a) core from 5.0 m; (b) core from 9.5 m, and (c) core from 21.8 m depth.

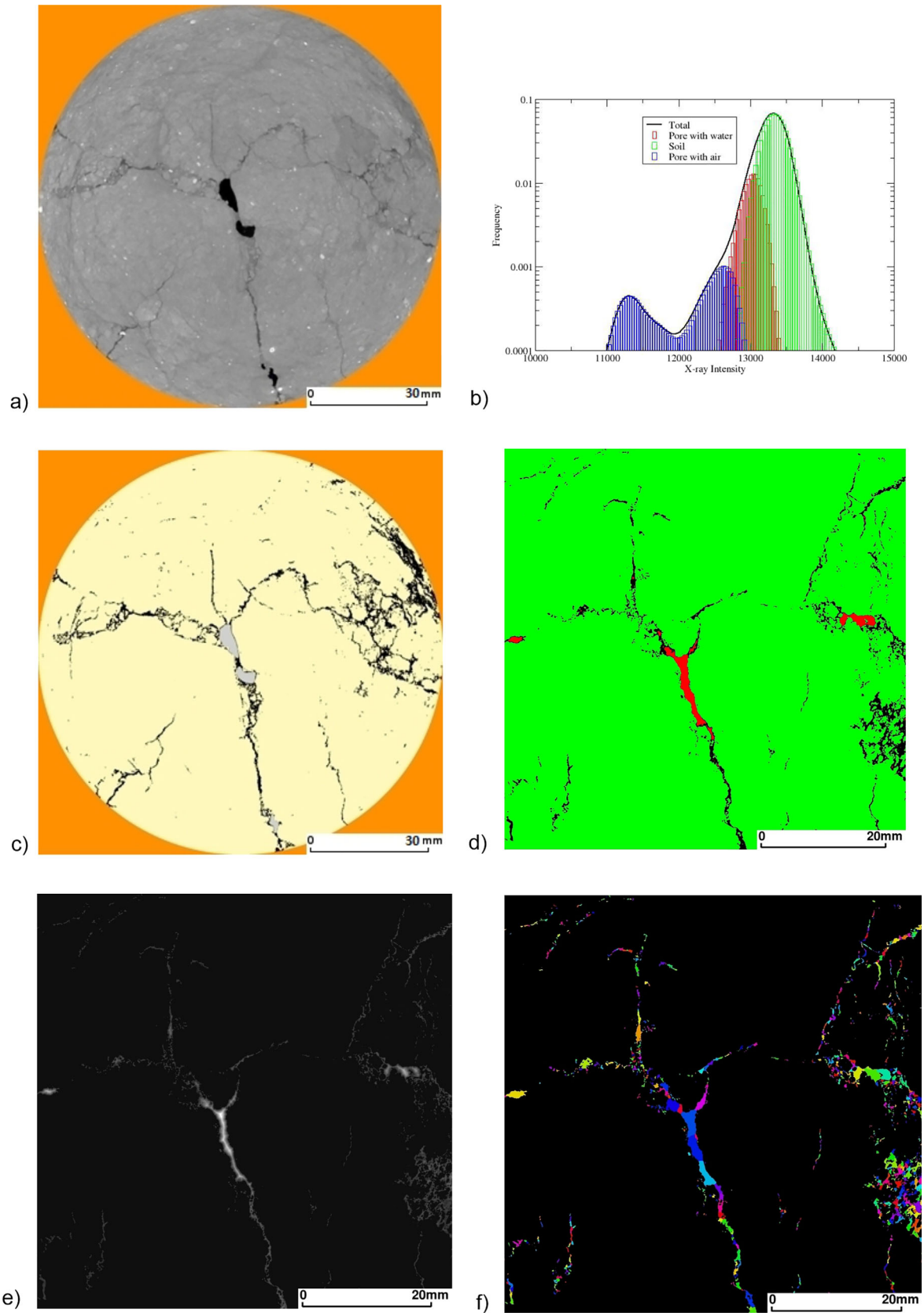

Figure 6. (continued)

Table 1
Volume Fraction of Segmented Phases in the Imaged 34 mm Length Core Subsample (Base From 19.25 m BGL)

Phase	Volume fraction
Water-filled pores	0.138
Soil	0.842
Gas-filled pores	0.012
Dense mineral	0.008

sediment with a high proportion of eolian silt-sized material. By contrast, the material from the vicinity of Cores 13 and 14 at approximately 19 m depth (75–80 ka) represents a much higher percentage of clay sized fraction and was initially logged as a 'massive clay' during drilling (Figure 2).

The PSD images show that a significant proportion of the nonclay size material in the sample from Core 3 (Figure 3) is a pale white angular material that has been identified as calcrete under microscopic examination. In contrast, the 250 and 500 μm samples from Core 13 are composed predominantly of subrounded quartz grains with some calcrete again occurring in Core 14 at these grain sizes. Calcrete can be seen in the soils forming on the eroded calc-alkali basalts at the southern margin of the Liverpool Plains. This material has been moved northward across the Plains (Figure 1) by major flood events in the past.

We interpret the PSD data and the photo micrographs of each of the PSD bins to indicate that the unit at this location has been assembled from varying sedimentary sources that have included: (a) fine to coarse sands eroded from the surrounding Triassic sandstone hills; (b) overbank clay deposits as the result of frequent flooding; and (c) calcrete grains eroded from the soil profile with the clay and aerial inputs of fine to coarse silt-size quartz. The predominance of each input has varied with changes in climate over the past 100 ka, a period that spans both the last interglacial warm period and the last glacial maximum. Sediments at 29 m BG at this site were deposited during the late Pleistocene (Acworth et al., 2015) corresponding with the maximum of the last interglacial. During this period, the climate was drying, dunes were growing in the arid interior of the continent, and the clay content across the landscape increased (Kelly et al., 2014; Young et al., 2002). During the Pleistocene, rainfall totals were similar to those currently (700 mm/a) (Kelly et al., 2014; Martin, 2006). There was no glaciation in this region.

The sedimentary succession clearly represents an environment where soil development has occurred repeatedly as sediment has been deposited on top of earlier sediment. Under these conditions, it is probable that paleosols and associated root networks from subaerial deposition will exist throughout the succession and will have been repeatedly buried by sediment sourced from successive floods. The sediments have hydraulic and macropore characteristics that reflect syndepositional palesol development within alluvial sediments. The hydraulic connectivity through this clayey deposit is expected to be higher than clays that are deposited by settling to the base of standing water bodies or other sedimentary deposits such as glacial tills or loess.

The root channels cannot be postdepositional because the grasses on the Plains have a rooting depth limited to approximately 1.2 m below surface. The native grassland (Plains grass) at the site are naturally devoid of trees that could otherwise account for deep root channels, except along creeks and rivers where scattered trees were documented by early explorers (Abbs & Littleboy, 1998). There is no evidence to suggest that tree cover became dominant on this grassy plain at any time in the past 100 ka (Martin, 2006).

4.2. Evidence for Preferential Flow Pathways

Visual dye tracing demonstrates that preferential flow pathways are present as submillimeter- to millimeter-scale sinuous channels, and that relatively high vertical K occurs to a depth of at least 31.4 m BGL (i.e., 31.4 m was the maximum core sampling depth). These results are consistent with evidence for dual porosity flow from interrupted flow experiments and modeling (Crane et al., 2015). Based on the morphology and

Figure 6. Image acquisition and processing of 2D horizontal slices: (a) 2D tomogram slice image after removing noise, through the center of the 3D tomogram of 34 mm length core subsample (base from 19.25 m BGL). This horizontal slice is at the top point of the macropore. The core was maintained in a sealed and saturated state after collection. The outer edge of the 101.6 mm diameter core is clearly seen. The calcrete and mineral fragments (Figure 4) appear as white grains; (b) intensity histogram depicting both the total intensity (black) and the individual intensity distributions of phases after segmentation; (c) Corresponding segmented image of the core depicting soil matrix (yellow), gas bubbles (gray), and water-saturated pore space (black); (d) Zoomed-in version of the segmented image depicting the gas phase in red; (e) Covering radius map as basis for pore partitioning (bright colors indicate large radii); and (f) Pore label image showing the segmentation of phases.

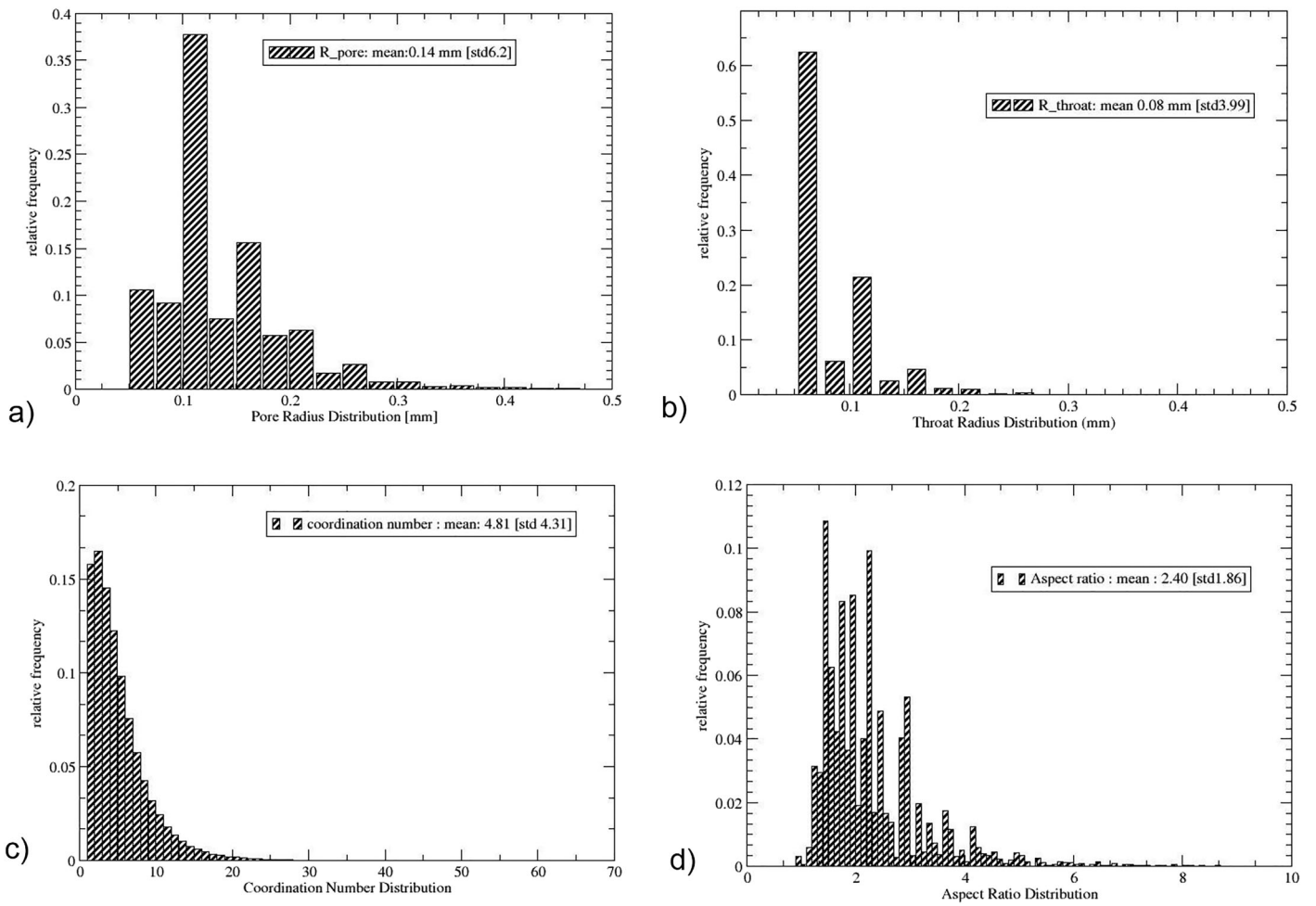

Figure 7. Pore network statistics of the central 2D horizontal slice of the 34 mm subsample (at the top point of the macropore) shown in Figure 6. (a) Pore radius distribution, (b) throat radius distribution, (c) coordination number distribution, and (d) pore-throat aspect ratio distribution.

scale of these channels, they are considered to be biogenic in origin, for example, paleo-rootholes. Root remains were not found during preparation of these samples but were noted during the microscope examination of other samples from the cores at depths of 1.0, 1.5, 2.0, 3.2, 14.0, and 15 m. Shell material, characteristic of moluscs living in fresh muddy water, was also recovered throughout the column. To the authors' best knowledge, the only other published work on this topic are those by White et al. (2008) and Emanuel and Sapsford (2016) where such syndepositional macropores were recorded to a depth of 2.0 m and ≈13 m, respectively.

The analysis of a single core subsample using the CT techniques described above lends independent support to the interpretation of the PSD and the dye tracer experiments. The CT analysis provides evidence of the high degree of connectivity between pores, and shows clear detail of the macropore morphology in a relatively large soil sample (34 mm length, 101.6 mm diameter). By comparison, CT analysis (Tracey et al., 2015) provided higher-resolution images of small soil sample cubes (10 × 10 mm), and determined that a representative element volume of 11 mm^3 was required to adequately characterize the hydraulic conductivity of soil pore structure. However, Tracey et al. (2015) noted that large macropores or voids would require further upscaling of hydraulic properties beyond this scale. In our study, the similarity between core-scale and site-scale *K* values suggests that the large (101.6 mm diameter) soil samples that were tested were a suitable size to provide realistic *K* values. If smaller samples were selected, there may have been a mismatch in *K* values between core scale and site scale (e.g., common 65 mm diameter drill core, or 10 mm diameter cores for high-resolution CT imaging).

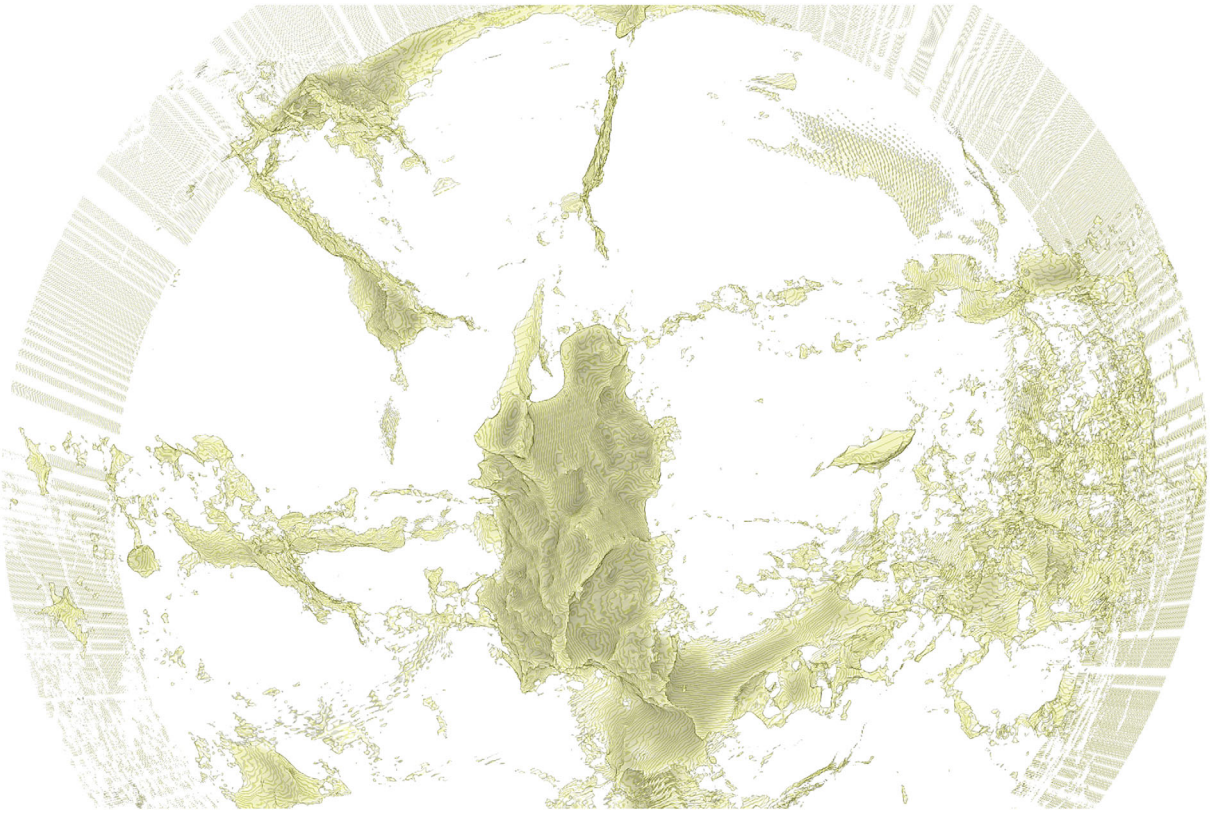

Figure 8. Three-dimensional visualization of the segmented gas phase of the total subsample (34 mm length, 101.6 mm diameter, base from 19.25 m BGL). This visualization shows the 3D morphology of the pores and the macropore.

Vertical connectivity through this material is provided both by connected pores (Figures 6 and 7) and by large macropores (Figure 8) that occur at depths significantly >10 m. Stresses at depths up to 31 m have not been sufficient to close these features, and geotechnical tests of cores from the same site indicated overconsolidated sediments (Bouzalakos et al., 2016). The cause of overconsolidation was not addressed (Bouzalakos et al., 2016), however, it can be speculated that repeated wetting and drying of the surface may have led to overconsolidation, because the area has not experienced loading due to glaciation.

The total porosity of water and gas-filled pores identified by CT imaging at a resolution of 49 μm was 15% (Table 1). By comparison, a total porosity of 43%–47% was measured, and a mobile domain (macroporosity) of 4%–8% was estimated from modeling, on cores from this site at a depth of 5.03, 9.52, and 21.75 m BGL (Crane et al., 2015). Sequential centrifuge permeability tests followed by CT imaging on additional cores are clearly warranted to verify the extent to which sample variability contributes to these results. The large macropore (Figure 8) is likely a similar feature to those observed during dye experiments. However, it was not possible to perform the CT analysis on exactly the same samples used in the dye experiments as these cores had been dissected for examination.

The CT imaging enabled discrimination of fluid and gas-filled porosity, showing that there is gas trapped below the water table within some of these macropores. It can be assumed that pores less than 49 μm size are water filled or the gas would not be trapped in the macropores (Mohammadian et al., 2015). Future investigations should consider the genesis and nature of this gas, for example, whether it may have been produced within the saturated zone by biochemical activity (Mohammadian et al., 2015). Further research is also needed to examine the effects of this small component (8% of pores, Table 1) of trapped gas on hydraulic conductivity values that are assumed to be at full saturation.

Preferential flow features have been reported by several authors (Greve et al., 2010b; Hinsby et al., 1996; McKay et al., 1993) who describe soil dessication leading to cracks and root development. These processes occur on the surface of the clay that is being eroded long after deposition. These postdepositional

processes are limited to the top of the unit being eroded. In contrast, the presence of syndepositional features could explain the rapid circulation of irrigation water from surface applications to a depth of 16 m Acworth and Timms (2009), at Breeza on the Liverpool Plains, although the clay-rich sediments at this site may be more heterogeneous than at the Cattle Lane site (Figure 1).

The evidence presented indicates that a high degree of pore connectivity occurs at the sample scale which, considered at site scale, means that the aquitard could be compromised by flow through connected pores and macropores. The vertical K of this thick smectite clay (in situ values and geometric mean of core samples), with connected pores and macropores would not comply with requirements for a hazardous waste landfills with $K < 10^{-9}$ m/s (*US-EPA*, 1989), despite the fact this aquitard is much thicker than constructed clay liners. The K of this clay matrix without macropores is likely $<10^{-10}$ m/s, the minimum K value that was measured on core from this site (26.1 m BGL; Timms et al., 2016). We detected pore characteristics that explain why there is a degree of connectivity at the core scale, although there is little evidence of direct connectivity at aquitard scale due to the lack of hydraulic gradient to drive flow and transport under current conditions (Acworth et al., 2015; Timms & Acworth, 2005).

We suggest that syndepositional processes are capable of establishing efficient pathways through the smectite-dominated clay material that would account for these observations. If this is the case, then all clay-dominated material that has accumulated subaerially could contain similar pathways that could compromise the integrity of such material as an aquitard. Recognition of this highlights the requirement to consider the paleo-environment under which the sediment was deposited. Further, this has significant implications for aquitards that may be assumed, in the absence of detailed investigation, to limit recharge, groundwater flow, and contaminant migration.

Macropores potentially compromise the integrity of aquitard because early breakthrough of contaminants could occur, relative to transport through a homogenous matrix that has a similar bulk hydraulic conductivity (Crane et al., 2015). Retardation due to diffusion of contaminants from the more mobile domain (macropores) to the less mobile domain (matrix or micropores) can be inferred from this work, and is commonly reported in literature (e.g., Jorgensen et al., 2004). Thus, dual porosity could result in potential early breakthrough and also a long tail of contaminant concentrations, relative to a homogeneous porous media. Another modeling approach, assuming an equivalent porous media model for transport through an aquitard, indicated that an order of magnitude reduction in vertical hydraulic conductivity would more than halve transport time (Timms & Hendry, 2008). Macropores do not occur in the glacial till aquitard that was modeled by Timms and Hendry (2008).

Thus, the possibility of macropores should be investigated beyond the near-surface soil zone at sites where contaminant migration is a risk. At the Cattle Lane site, the integrity of these saturated clayey deposits could be compromised by the transport of salt from the shallow zone downwards through the aquitard, if a vertical hydraulic gradient was applied by groundwater extraction from the underlying aquifer.

4.3. Limitations and Further Work

Further work is required to evaluate the effects of trapped gas (8% of pores in Table 1) on preferential flow and hydraulic conductivity values that were assumed to be at full saturation. CT imaging and digital analysis should be repeated on cores, sequentially after K and dye tracer testing, with subcoring and dual-contrast reagents to increase CT image resolution, distinguish between clay minerals and other solid matrix and evaluate scaling effects on hydraulic properties. Distinguishing between matrix flow and preferential flow via connected pores and macropores requires further work. The search for organic and biochemical evidence of root systems should continue, although oxidized conditions may not be favorable for preservation (Martin, 2006). The large diameter core hole (101.6 mm) through this aquitard, while revealing valuable data and information on groundwater processes, should be repeated at additional representative locations if plans to depressurize the underlying aquifer are proposed, and hence risk migration of contaminants.

5. Conclusions

Using particle size distribution analyses, microscopic photography, dye tracer testing and micro CT-based sample characterization performed on sediment core material within a layered clay sequence, we demonstrate that preferential flow pathways can exist throughout the depth of an aquitard sequence. We further

illustrate that, if the sedimentation has occurred subaerially, this depositional process produces an entirely different set of sedimentary characteristics to those acquired by sedimentation beneath fresh or salt water.

Preferential flow pathways exist through the presence formed by old root holes that provide channels or, perhaps more significantly, through buried macropores. It is apparent that the macropores must have been preserved by the rapid addition of further material during floods. These syndepositional features are distinct from the postdepositional features (e.g., fracturing due to stress relief on unloading, dessication cracks, root channel) that can only be generated close to a surface subject to unloading and weathering.

Our results demonstrate that the integrity of aquitards that include syndepositional macropores and connected pores within a fine matrix can clearly be compromised. We further illustrate the value of combining multiple techniques, such as geotechnical centrifuge tracer experiments with CT imaging, when investigating the characteristics of aquitard forming materials. Our findings have significant implications for future aquitard characterization studies by highlighting the critical necessity to study both the paleo-environment and bulk lithology of an aquitard. For example, it is likely that, if identified, the presence of syndepositional features will require modification of any conceptual model of these aquitards. This has clear implications for any case where aquitards are assumed to act as a natural hydraulic barrier.

Acknowledgments
We would like to thank Mark Whelan from the UNSW School of Mining Engineering and Connected Waters Initiative, Australia, for his technical support. The work was financially supported by the National Centre for Groundwater Research and Training, supported by the Australian Research Council and the National Water Commission. Mark Cuthbert was financially supported by the European Community Seventh Framework Programme (FP7/2007–2013) under grant agreement 299091. C.H.A. acknowledges funding by the Australian Research Council through an ARC Future Fellowship (FT120100216). This research was undertaken with the assistance of resources provided at the NCI National Facility systems through the National Computational Merit Allocation Scheme supported by the Australian Government (m65). Data that are used to generate graphs in this paper can be accessed here: https://doi.org/10.6084/m9.figshare.5830317.v1 and https://doi.org/10.6084/m9.figshare.5821257.v1.

References

Abbs, K., & Littleboy, M. (1998). Recharge estimation for the Liverpool Plains. *Australian Journal of Soil Research*, *35*, 335–357.

Acworth, R. I., Halloran, L., Rau, G., Cuthbert, M., & Bernadi, T. (2016). An objective method to quantify groundwater compressible storage using earth and atmospheric tides. *Geophysical Research Letters*, *43*, 11,671–11,678. https://doi.org/10.1002/2016GL071328

Acworth, R. I., Rau, G. C., Halloran, L. J. S., & Timms, W. A. (2017). Vertical groundwater storage properties and changes in confinement determined using hydraulic head response to atmospheric tides. *Water Resources Research*, *53*, 2983–2997. https://doi.org/10.1002/2016WR020311

Acworth, R. I., & Timms, W. (2009). Evidence for connected water processes through smectite-dominated clays at Breeza, New South Wales. *Australian Journal of Earth Sciences*, *56*(1), 81–96. https://doi.org/10.1080/08120090802541952

Acworth, R. I., Timms, W., Kelly, B., McGeeney, D., Ralph, T., Larkin, Z., & Rau, G. (2015). Late Cenozoic paleovalley fill sequence from the Southern Liverpool Plains, New South Wales—Implications for groundwater resource evaluation. *Australian Journal of Earth Sciences*, *62*, 657–680. https://doi.org/10.1080/08120099.2015.1086815

Arns, C., Bauget, F., Ghous, A., Sakellariou, A., Senden, T., Sheppard, A., & Sok, R. (2005a). Digital core laboratory: Petrophysical analysis from 3D imaging of reservoir core fragments. *Petrophysics*, *46*(4), 260–277.

Arns, C. H., Knackstedt, M. A., & Martys, N. S. (2005b). Cross-property correlations and permeability estimation in sandstone. *Physical Review E—Statistical, Nonlinear, and Soft Matter Physics*, *72*(4), 046304. https://doi.org/10.1103/PhysRevE.72.046304

Arns, J., Sheppard, A., Arns, C., Knackstedt, M., Yelkhovsky, A., & Pinczewski, W. (2007). Pore-level validation of representative pore networks obtained from micro-CT images. Paper presented at the International Symposium of the Society of Core Analysts, Calgary, Canada, September 10–12.

Bernabe, Y., Li, M., Tang, Y., & Evans, B. (2016). Pore space connectivity and the transport properties of rocks. *Oil Gas Science and Technology*, *71*, 50.

Blott, S. J., & Pye, K. (2001). Technical communication Gradistat: A grain size distribution and statistics package for the analysis of unconsolidated sediments. *Earth Surface Processes and Landforms*, *1248*, 1237–1248.

Botha, P. W., & Sheppard, A. P. (2016). Mapping permeability in low-resolution micro-CT images: A multiscale statistical approach. *Water Resources Research*, *52*(6), 4377–4398. https://doi.org/10.1002/2015WR018454

Bouzalakos, S., Crane, R., McGeeney, D., & Timms, A. (2016). Stress-dependent hydraulic properties of clayey-silt aquitards in eastern Australia. *Acta Geotechnica*, *11*, 969–986.

Busacca, A. (1989). Long quaternary record in eastern Washington, U.S.A., interpreted from multiple buried paleosols in loess. *Geoderma*, *45*(2), 105–122.

Crane, R., Cuthbert, M., & Timms, W. (2015). Technical note: The use of an interrupted-flow centrifugation method to characterise preferential flow in low permeability media. *Hydrology and Earth System Sciences*, *19*(9), 3991–4000. https://doi.org/10.5194/hess-19-3991-2015

Cuthbert, M. O., Mackay, R., Tellam, J. H., & Barker, R. D. (2009). The use of electrical resistivity tomography in deriving local-scale models of recharge through superficial deposits. *Quarterly Journal of Engineering Geology and Hydrogeology*, *42*(2), 199–209. https://doi.org/10.1144/1470-9236/08–023

Cuthbert, M. O., Mackay, R., Tellam, J. H., & Thatcher, K. E. (2010). Combining unsaturated and saturated hydraulic observations to understand and estimate groundwater recharge through glacial till. *Journal of Hydrology*, *391*(3–4), 263–276. https://doi.org/10.1016/j.jhydrol.2010.07.025

Cuthbert, M. O., & Tindimugaya, C. (2010). The importance of preferential flow in controlling groundwater recharge in tropical Africa and implications for modelling the impact of climate change on groundwater resources. *Journal of Water and Climate Change*, *1*(4), 2234–2245. https://doi.org/10.2166/wcc.2010.040

Emanuel, D., & Sapsford, D. (2016). Fossil rootlet biopores as conduits for contaminant transport through clay horizons: A case study of DNAPL behaviour in Severn alluvium, UK. *Environmental Earth Science*, *75*(11), 972. https://doi.org/10.1007/s12665-016-5756-5

Gocke, M., Huguet, A., Derenne, S., Kolb, S., Dippoldd, M., & Wiesenberg, G. (2017). Disentangling interactions between microbial communities and roots in deep subsoil. *Science of the Total Environment*, *575*, 135–145.

Greve, A., Acworth, R., & Kelly, B. (2010a). Detection of subsurface soil cracks by vertical anisotropy profiles of apparent electrical resistivity. *Geophysics*, *75*, WA85–WA93.

Greve, A., Andersen, M. S., & Acworth, R. I. (2010b). Investigations of soil cracking and preferential flow in a weighing lysimeter filled with cracking clay soil. *Journal of Hydrology*, *393*(1–2), 105–113. https://doi.org/10.1016/j.jhydrol.2010.03.007

Greve, A., Andersen, M. S., & Acworth, R. I. (2012). Monitoring the transition from preferential to matrix flow in cracking clay soil through changes in electrical anisotropy. *Geoderma*, *179–180*, 46–52.
Hinsby, K., McKay, L., Jorgensen, P., Lenczewski, M., & Gerba, C. (1996). Fracture aperture measurements and migration of solutes, viruses, and immiscible Creosote in a column of Clay-Rich Till. *Groundwater*, *34*(6), 1065–1075. https://doi.org/10.1111/j.1745-6584.1996.tb02172.x
Hoshen, J., & Kopelman, R. (1976). Percolation and elastic distribution 1 Cluster multiple labeling techniques and critical concentration algorithm. *Physical Review B*, *14*(8), 3438–3445.
Jorgensen, P., Broholm, K., Sonnenborg, T., & Arvin, E. (1998). DNAPL transport through macroporous, clayey till columns. *Ground Water*, *36*, 651–660.
Jorgensen, P., Helstrup, T., Urup, J., & Seifert, D. (2004). Modeling of non-reactive solute transport in fractured clayey till during variable flow rate and time. *Journal of Contaminant Hydrology*, *68*(3–4), 193–216.
Jorgensen, P., Hoffmann, M., Kistrup, J., & Bryde, C. (2002). Preferential flow and pesticide transport in a clay rich till: Field, laboratory and modelling analysis. *Water Resources Research*, *38*(11), 1246. https://doi.org/10.1029/2001WR000494
Kelly, B. F., Timms J. W., Ralph, T., Giambastiani, B., Comunian, A., McCallum, A., et al. (2014). A reassessment of the Lower Namoi catchment aquifer architecture and hydraulic connectivity with reference to climate drivers. *Australian Journal of Earth Sciences*, *61*, 501–511.
Klint, K., & Gravesen, P. (1999). Fracture and biopores in Weichselian clayey till aquitards at Flakkebjerg, Denmark. *Nordic Hydrology*, *30*, 267–284.
Knackstedt, M., Arns, C., Ghous, A., Sakellariou, A., Senden, T., Sheppard, A., et al. (2006). 3D imaging and flow characterisation of the pore space of carbonate core samples. Paper presented at International Symposium of the Society of Core Analysts held in Trondheim, Norway, September 12–16.
Larue, D. K., & Hovadik, J. (2006). Connectivity of channelized reservoirs: A modelling approach. *Petroleum Geoscience*, *12*(4), 291–308. https://doi.org/10.1144/1354-079306-699
Lenormand, R., Zarcone, C., & Sarr, A. (1983). Mechanisms of the displacement of one fluid by another in a network of capillary ducts. *Journal of Fluid Mechanics*, *135*, 337–353. https://doi.org/10.1017/S0022112083003110
Limaye, A. (2012). Drishti: A volume exploration and presentation tool. In S. R. Stock (Ed.), *Developments in x-ray tomography VIII, Proceedings SPIE* (Vol. 8506). Canberra: Australian National University.
Martin, H. (2006). Cenozoic climatic change and the development of the arid vegetation in Australia. *Journal of Arid Environments*, *66*, 533–563.
McKay, L. D., Cherry, J. A. & Gillham, R., W. (1993). Field experiments in a fracture clay till 1. Hydraulic conductivity and fracture aperture. *Water Resources Research*, *29*(4), 1149–1162.
Mohammadian, S., Geistlinger, H., & Voge, H. (2015). Quantification of gas-phase trapping within the capillary fringe using computed microtomography. *Vadose Zone Journal*, *14*(5), vzj2014.06.0063.
Neuzil, C. (1994). How permeable are clays and shales? *Water Resources Research*, *30*(2), 145–150.
O'Geen, A., McDaniel, P., Bollc, J., & Keller, C. (2005). Paleosols as deep regolith: Implications for ground-water recharge across a loessial climosequence. *Geoderma*, *126*, 85–99.
O'Hara, S., Parker, B., Jorgensen, P., & Cherry, J. (2000). Trichloroethene DNAPL flow and mass distribution in naturally fractured clay: 1. Evidence of fracture aperture variability. *Water Resources Research*, *36(1)*, 135–147.
Rudolph, D., Cherry, J., & Farvolden, R. (1991). Groundwater flow and solute transport in a fractured lacustrine clay near Mexico City. *Water Resources Research*, *27*(9), 2187–2201. https://doi.org/10.1029/91WR01306
Sheppard, A., Sok, R., & Averdunk, H. (2004). Techniques for image enhancement and segmentation of tomographic images of porous materials. *Physica A: Statistical Mechanics and Its Applications*, *339*(1), 145–151.
Sheppard, A., Sok, R., & Averdunk, H. (2005). Improved pore network extraction methods. In A. Sheppard, R. Sok, and H. Averdunk (Eds.), *Core analysis soultions across scales and disciplines* (p. P021). Toronto, Canada: Society of Core Analysts.
Timms, W. A., & Acworth, R. I. (2005). Propagation of porewater pressure change through thick clay sequences: An example from the Yarramanbah site, Liverpool Plains. *Hydrogeology*, *13*, 858–870.
Timms, W. A., & Hendry, M. (2008). Long-term reactive solute transport in an aquitard using a centrifuge model. *Ground Water*, *46*(4), 616–628. https://doi.org/10.1111/j.1745-6584.2008.00441.x
Timms, W., Crane, R., Anderson, D. J., Bouzalakos, S., Whelan, M., McGeeney, D., et al. (2016). Accelerated gravity testing of aquitard core permeability and implications at formation and regional scale. *Hydrology and Earth System Sciences*, *20*(1), 39–54. https://doi.org/10.5194/hess-20–39-2016
Tracey, S. R., Daly, C. J., Sturrock, K. R., Crout, N. M., & Mooney, S. J. (2015). Three-dimensional quantification of soil hydraulic properties using X-ray Computed Tomography and image-based modeling. *Water Resources Research*, *51*, 1006–1022. https://doi.org/10.1002/2014WR016020
US-EPA. (1989). *Requirement for hazardous waste landfill design, construction and closure* (Tech. Rep. EPA/625/4–89/022). Washington, DC: U.S. Environmental Protection Agency.
Vulava, V., McKay, L., Driese, S., Menn, F., & Sayler, G. (2007). Distribution and transport of coal tar-derived PAHs in fine grained residuum. *Chemosphere*, *68*, 554–563.
Wealthall, G. P., Steele, A., Bloomfield, J. P., Moss, R. H., & Lerner, D. N. (2001). Sediment filled fractures in the Permo-Triassic sandstones of the Cheshire Basin: Observations and implications for pollutant transport. *Journal of Contaminant Hydrology*, *50*(1–2), 41–51. https://doi.org/10.1016/S0169-7722(01)00104-8
White, R. A., Rivett, M. O. & Tellam, J. H. (2008). Paleo-roothole facilitated transport of aromatic hydrocarbons through a Holocene clay bed. *Environmental Science and Technology*, *42*(19), 7118–7124. https://doi.org/10.1021/es800797u
Young, R. W., Young, A. R. M., Price, D. M., & Wray, R. A. L. (2002). Geomorphology of the Namoi alluvial plain, northwestern New South Wales. *Australian Journal of Earth Sciences*, *49*, 509–523.